Icarus **151**, 51–68 (2001)
doi:10.1006/icar.2001.6596, available online at http://www.idealibrary.com on IDEAL®

Comprehensive Photometry of the Rings and 16 Satellites of Uranus with the Hubble Space Telescope[1]

Erich Karkoschka

Lunar and Planetary Laboratory, University of Arizona, Tucson, Arizona 85721-0092
E-mail: erich@pirl.lpl.arizona.edu

Received July 27, 1999; revised November 15, 2000

Photometric properties of 4 rings and 16 satellites of Uranus are presented, based on 41 Hubble Space Telescope images taken in 1997. Up to 25 filters per object covered the wavelength range 0.27–2 μm. The whole range of phase angles observable from Earth (0.03–3°) was probed. Reflectivities were calibrated on an absolute scale to typically 4% accuracy. Below 1 μm, derived geometric albedos of major satellites are typically 30% higher than previously reported due to previously unobserved steep upturns of the phase curve shortward of 0.2° phase angle, possibly caused by coherent backscatter. Portia is slightly oblong and Juliet and Belinda are very oblong based on their rotational lightcurves. Puck displays a weak spectral feature indicative of water ice absorption. Cordelia and Ophelia were recovered very close to the positions predicted from their gravitational influence on the ε ring. They have not been observed since 1986. Subtle color variations within the satellite system were confirmed. Throughout the uranian system, the slope of phase curves below 1° phase angle displays a strong correlation with the albedo and a strong anticorrelation with the slope at higher phase angles. Similar correlations were found for Hapke parameters. The brightness of 20 members of the uranian system is presented in functional form for a wide range of wavelengths, phase angles, and orbital longitudes.

Key Words: rings of Uranus; satellites of Uranus; photometry; spectrophotometry.

I. INTRODUCTION

The encounter of Voyager 2 with Uranus in 1986 provided an enormous leap in our understanding of the uranian system. Nevertheless, ground-based data are still complementary to the Voyager data since they cover the opposition surge at small phase angles (Goguen *et al*. 1989, Buratti *et al*. 1992), they cover the infrared (Herbst *et al*. 1987, Baines *et al*. 1998), and they span decades (Lockwood and Thompson 1999).

Recent observations by the Hubble Space Telescope (HST) yielded major advances because of better spatial resolution than ground-based data and because of sampling of wavelengths and phase angles not observed by Voyager 2. Pascu *et al*. (1995) reported the first color data on minor satellites. Based on six HST images, Karkoschka (1997) determined colors for further satellites and found geometric albedos of ring particles and minor satellites to be 50–90 percent higher than estimations based on Voyager images. A more extensive observing program in 1997 yielded surprising results for Uranus (Karkoschka 1998a). The analysis of the same exposures with respect to ring and satellite photometry is the main topic of this work.

This work provides photometric properties of the individual rings and satellites of the uranian system. The analysis spans the complete range of viewing geometries available, while simultaneously covering the entire wavelength range from 0.27 to 2 μm. For completeness, the unique Voyager images were included, which provide in particular high-phase angle data unobtainable from Earth. Such a comprehensive investigation of the uranian system yielded several unexpected yet enlightening results.

This work covers the whole regular uranian system which includes the rings, 5 large major satellites, and 11 small minor satellites including a satellite discovered in 1999, S/1986 U 10, but excludes satellites with large, highly inclined, and eccentric orbits discovered recently (Gladman *et al*. 1998).

Section II describes the photometric calibration. Section III gives a revised classification of uranian objects according to surface types. Section IV explains the adopted photometric model and gives all parameters. Sections V through VIII discuss the results for rotational lightcurves, phase functions, spectral slopes, and spectral absorptions. Section IX gives a physical interpretation of the phase functions. Section X discusses recovery of faint satellites. Section XI summarizes the main results.

II. CALIBRATION

The main data set of this work consists of 41 HST images of Uranus taken for the observing program GO 7429 by Tomasko and Karkoschka with the WFPC2 and NICMOS cameras. The phase angles cover the complete range accessible from Earth (Table I). The finite size of the sun was neglected since it only

[1] Based on observations with the NASA/ESA Hubble Space Telescope obtained at the Space Telescope Science Institute, which is operated by the Association of Universities for Research in Astronomy, Inc., under NASA Contract NAS5-26555.

0019-1035/01 $35.00

TABLE I
Observation Log

#	Phase angle (°)	Camera (s)	Date 1997	SubEarth latitude (°)	Subsolar latitude (°)
1	0.034	PC1	Jul 29.96	−40.4	−40.3
2a	0.079	NIC1,2	Jul 28.40	−40.3	−40.4
2b	0.081	NIC2	Jul 28.34	−40.3	−40.4
3	0.21	PC1, WF2	Jul 25.66	−40.2	−40.4
4	1.10	PC1, WF4	Jul 7.57	−39.5	−40.6
5	2.82	PC1	Oct 16.07	−42.3	−39.5

increases the smallest phase angle effectively by 0.001°. The image scale varied between 590 and 1370 km/pixel. One orbit of imaging occurred on each of five dates. Subsolar and subearth latitudes (Table I) are defined here as the angles of the incoming/outgoing light rays with the equatorial plane of Uranus. Since all orbits of rings and orbits and equators of regular uranian satellites (as far as known) are aligned with Uranus' equator to better than 0.5° (except 4° for Miranda), the quantities of Table I apply throughout the regular uranian system.

Each filter is named in this work according to its mean wavelength (Table II). Red leaks in the 0.32 and 0.34 μm filters (∼2%) were subtracted based on data in red filters. The sampling of wavelengths and phase angles is good below 1 μm wavelength where the spectrum and the phase dependence can be determined independently (Table II, last column).

The four long integrations (560 s) were split into 160 and 400 s exposures in order to facilitate identification of pixels hit by cosmic rays. For these exposure pairs, the mean and scatter of measured signal ratios were 2.51 ± 0.01 (for the 4 images of Uranus) and 2.51 ± 0.04 (for the 10 brightest satellite images), close to the expected value of 2.5 and thus confirming linearity. Both integrations on NIC1 were split into two exposures of equal length with Uranus centered on different parts of the chip.

Many exposures contain the whole regular uranian system on the PC1 chip. This can be done only if the outermost satellites are all on the same side of Uranus. The observations were scheduled accordingly. An example is shown in Fig. 1. On the other hand, the field of view of NICMOS allows only simultaneous imaging of the uranian system out to Ariel. Titania was imaged on a different chip than Uranus. For completeness, NICMOS data from 1998 observations of Umbriel by Smith *et al*. (GO 7183) and of Oberon by Hammel *et al*. (GO 7885) are included in Sections VII–IX.

Most WFPC2 exposures had maximum exposure levels within a factor of two below the saturation level. WFPC2 exposures with much lower exposure levels (filters 0.27, 0.89, and 0.95 μm) were recorded at the lower gain setting in order to minimize the digitization error. Data for Ariel and Titania in the 1.59 μm filter are based on the readouts within the first half of the exposure time since they saturated later into the exposure.

Pixels contaminated by cosmic ray hits, about 60,000 pixels or 0.2% of all pixels, were replaced by interpolation using an automated routine with manual intervention in questionable cases (Fig. 1). Special care was given to areas close to the rings and satellites. The final calibrated image in the calibration pipeline of the Space Telescope Science Institute (STScI) is called the raw image in this work because it is the starting point for this work.

Deconvolution

The raw images were deconvolved with the Wiener or Fourier method (cf. Magain *et al*. 1997). Unlike other deconvolution techniques (e.g., the Lucy method, Lucy 1974), it preserves integrated photometric values. It does not try to create an image of perfect resolution. It gives a different, deterministic representation of the image according to a specified point spread function (PSF). The method works well only if the specified PSF has the same cutoff frequency as the original PSF. If the cutoff frequency is higher, the solution blows up and the result is a noisy, less useful image. If the cutoff frequency is lower, some information is lost, and the reverse transformation (convolution) will not exactly retrieve the original image. While there is only one recommended cutoff frequency for the specified PSF, the choice of the shape of the specified PSF is unlimited.

TABLE II
Filter Data

Mean wavelength (μm)	Filter name	CCD	Signal (e^-)	Integration time (s)	Dates
0.27	F255W	PC1	<1	560	- - 3 - -
0.32	F300W	PC1	5	160	- - - 4 -
0.34	F336W	PC1	16	2 × 160	1 - - - 5
0.41	F380W	PC1	8	40	- - 3 - -
0.43	F439W	PC1	8	35	- - - 4 -
0.47	F467M	PC1	6	60	- - - - 5
0.54	FQCH4N-A	WF2	2	40	- - 3 - -
0.55	F547M	PC1	10	10	1 - - - -
0.59	F588N	PC1	6	80	- - - - 5
0.62	FQCH4N-B	PC1	35	560	- - - 4 -
0.63	F631N	PC1	13	2 × 100	1 - - - 5
0.66	F658N	PC1	10	160	- - 3 - -
0.67	F673N	PC1	16	160	1 - - - -
0.73	FQCH4N-C	WF4	10	160	- - - 4 -
0.78	F791W	PC1	35	26	- - - 4 -
0.86	F785LP	PC1	160	80,160	- - 3 - 5
0.89	FQCH4N-D	PC1	11	560	1 - - - -
0.91	F850LP	PC1	250	4 × 160	1 - 3 4 5
0.95	F953N	PC1	5	560	- - - - 5
1.08	F108N	NIC1	20	384	- 2 - - -
1.59	F160W	NIC2	900	2 × 128	- 2 - - -
1.64	F165M	NIC1	400	256	- 2 - - -
1.72	F171M	NIC2	160	2 × 128	- 2 - - -
1.87	F187W	NIC2	400	2 × 128	- 2 - - -
2.03	F204M	NIC2	180	2 × 176	- 2 - - -

Note. Signal is the total signal expected from S/1986 U 10, the faintest satellite. The numbering of dates is the same as in Table I.

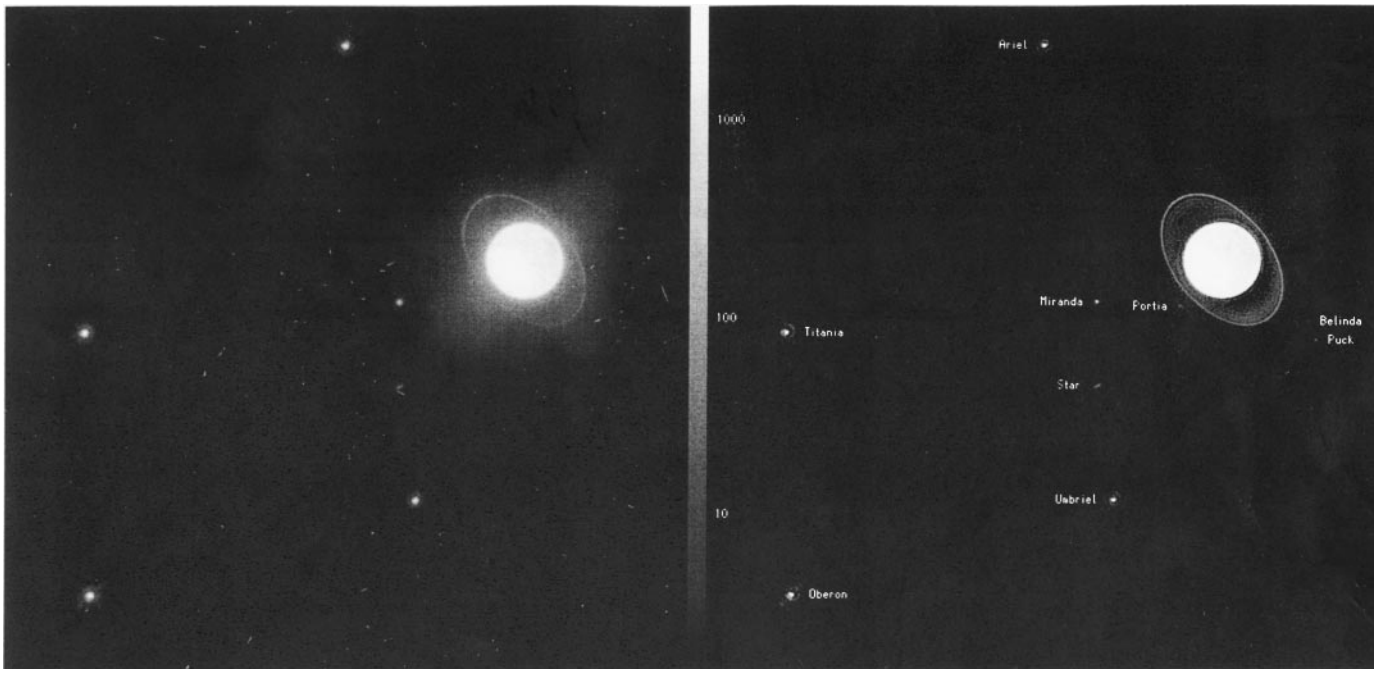

FIG. 1. Raw image (left) and deconvolved image with contamination by cosmic ray hits removed (right) at 0.91 μm at 1.1° phase angle. The displayed brightness is on a logarithmic scale as indicated by the bar separating the images. Data numbers are listed at the bar.

For this work, the specified PSF was the Fourier transform of the amplitude function $(1 - k^2/k_o^2)^5$ for $k < k_o$ and zero otherwise, where k is the spatial frequency and k_o is the cutoff frequency, depending on the filter. Exponents well below 5 in the function above yield undesirable "ringing," while exponents well above 5 approximate Gaussians with less desirable long wings. The specified PSF has strongly reduced wings causing a reduction of large halos around bright objects (cf. Fig. 1). The PSF for the raw image was generated by the TinyTim Software of STScI by Krist (1994) and was slightly adjusted since the STScI software does not account for the large angle scattering (Fig. 5.9 of Biretta *et al*. 1996).

Deconvolution with the Fourier method does not change the signal-to-noise ratio for each spatial frequency. The full width at half maximum (FWHM) of the PSF, sometimes called the spatial resolution, changes by the deconvolution shown in Fig. 1 insignificantly from 0.085″ to 0.09″.

Aperture Photometry

The workings of deconvolution can be seen in an example of aperture photometry on the images of Uranus and the satellite Miranda in Fig. 1. All data numbers (DN) within a certain radius were summed up after the sky background had been subtracted as estimated from an annulus around the aperture. The annulus, separated by 0.1″ from the aperture, had a width of $0.2'' + r/2$ where r is the radius of the aperture. No sky subtraction was required for Uranus because of the lack of other bright objects in the image.

For apertures between 0.1 and 0.5″ radius, the data points in Fig. 2 follow their expected, plotted curves, based on aperture photometry of the PSFs. STScI usually uses 0.5″ for photometry (Keyes 1997). Beyond 0.5″, Miranda's data points deviate from the predicted curves because the annulus and the aperture run into the diffraction pattern of Uranus. For the deconvolved image, the deviations are typically 10 times less.

The faintest satellite measured in Fig. 1 is 250 times fainter than Miranda and closer to Uranus where the background is brighter. Thus, an insignificant 1% error for a 0.5″ aperture on

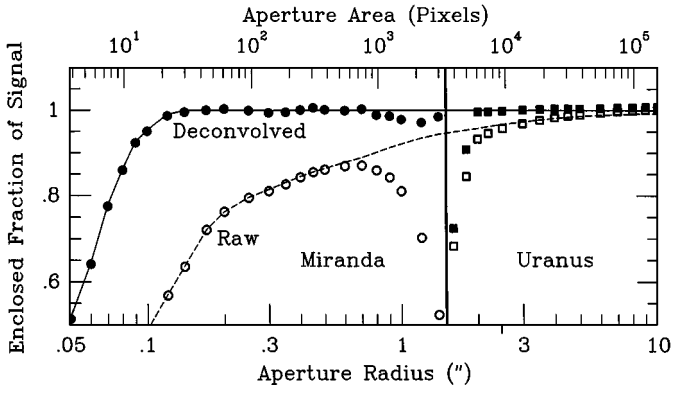

FIG. 2. Aperture photometry for the raw and deconvolved images (open and filled circles/squares, respectively) on Miranda and Uranus (left and right panel, respectively). The theoretical functions are indicated by the dashed and solid curves.

Miranda caused by a background feature would be a 250% error in the measurement of the faint satellite. While such large errors can be decreased by reducing the aperture size, the improvement by a factor of ~10 due to deconvolution is clearly crucial. Photometric measurements with ground-based telescopes usually employ apertures of 2–4″ radius while Miranda requires apertures less than 1″ according to Fig. 2. Thus, there is very little ground-based data for Miranda at similar wavelengths while HST can go some 250 times fainter.

In the raw and deconvolved images, 99% of the light is contained in aperture areas of 100,000 and 20 pixels, respectively, a decrease by a factor of 5,000. This great improvement enabled the photometric separation of individual rings and satellites from Uranus.

The deconvolution was performed with a PSF for the position of Uranus which works well in the area around Uranus. Far from Uranus, fringes around the satellites (cf. Fig. 1, right panel) contain a few percent of the signal which hardly mattered because of the choice of large apertures.

All photometric data in this work come from deconvolved images with the aperture dependent on the brightness of the satellite image, which ranged from 0.08″ (faint images) to 0.5″ (bright images). In order to predict the fractional signal in each aperture and to correct for it, all PSFs were smeared according to the satellite's size and motion during the exposure (both typically 1 pixel or less). For Uranus, an aperture of 2.1″ radius was chosen.

The brightness of rings was initially measured in a way similar to aperture photometry with background inside and outside the rings fitted to a linear or quadratic function of distance from Uranus. Because of overlapping PSFs between different rings, these values needed adjustments once the contributions from the other rings were taken into account. Large error bars are associated with data at longitudes close to Uranus, which then hardly contribute to the measured error-weighted averages.

Intensity Calibration

The reflectivity is the I/F averaged over the whole disk at a specific phase angle α, denoted here as I_α/F. There are two methods to convert DN into reflectivity, both of which are used here. The first one uses flux calibrations by STScI for each filter (Karkoschka 1998b).

The second method uses an imaged object with known reflectivity, in this work Uranus and its geometric albedo spectrum shortward and longward of 0.3 μm wavelength (Wagener *et al*. 1986 and Karkoschka 1998c, respectively). The former were scaled to the adopted equatorial radius of Uranus, 25,559 km. All albedos were adjusted according to the expected geometric change between 1995 and 1997, assumed to be similar to the observed change between 1993 and 1995 (Karkoschka 1998c). Up to 5% darkening is expected at wavelengths where Uranus' receding polar region is bright.

Published reflectivities are dependent on the assumed brightness of the sun. This work assumes a magnitude of the sun at a unit distance of V = −26.75 (Hayes 1985). Since Karkoschka (1998c) assumed a value of −26.74, those reflectivities were scaled down by 1%. On the other hand, STScI uses a slightly different flux calibration corresponding to a solar magnitude between −26.77 (Biretta *et al*. 1996, Section 8.7) and −26.79 (Axon *et al*. 1996, p. 257) using the solar flux in V by Colina *et al*. (1996 and references therein). Thus, the STScI-based reflectivity calibration was increased by 3% to match the solar magnitude assumed for this work.

These two calibration methods are compared for the geometric albedo of the major satellites with data scaled to 0° phase angle as described in Section VI. Figure 3 displays their average which has a precision of 1.5%. A few times, a missing data point for one of the satellites had to be estimated for this plot based on satellite intensity ratios at nearby wavelengths.

Quadratic fits to both data sets, plotted in Fig. 3, agree within 1% over a major part of the wavelength range. The data points for each filter scatter by 5% (STScI calibration) and by 1.5% (Uranus calibration). A 5% scatter for many of the WFPC2 filters (mostly narrow ones) is consistent with expectations (Biretta 1998, personal communication). Based on this comparison, the adopted calibration for this work was halfway between the Uranus calibration (solid circles in Fig. 3) and the smoothed STScI calibration (dashed line), deviating on average by only 1% from either one.

The six NICMOS filters beyond 1 μm wavelength were calibrated with the first method (STScI) since the spectra of the major satellites are not smooth in this wavelength range, and since there is no suitable spectrum of Uranus. Therefore, the calibration beyond 1 μm is less reliably established. These filters have a calibration accuracy of 2–4% (Dickinson 1999).

The charge-transfer efficiency and the nonlinearity of the WFPC2 camera was applied for each object based on equations given by Whitmore and Heyer (1997) and Biretta *et al*. (1996). For the brighter satellites, the correction was typically 1–2%. For the faintest satellites, the correction occasionally exceeded 10%. The WFPC2 has been photometrically quite stable (Baggett

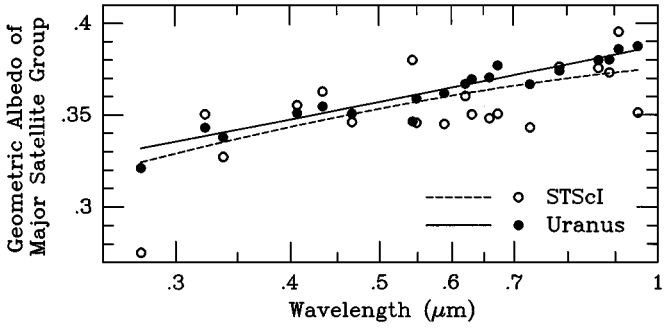

FIG. 3. Geometric albedos of the major satellite group in WFPC2 filters if calibrated with STScI data (open circles) and if calibrated with the albedo of Uranus (solid circles). Quadratic fits to the data are shown by dashed and solid curves. The geometric albedo of the satellite group is defined here as the total light divided by the total area.

TABLE III
Adopted Integrated Cross Sections of Ring Particles (10^6 km^2)

	Phase angle			
Ring group	<0.1°	0.21°	1.10°	2.82°
6, 5, 4	0.43	0.43	0.42	0.43
α, β	1.13	1.12	1.10	1.12
η, γ, δ	1.44	1.43	1.39	1.40
ε	7.64	7.56	7.18	7.07

and Gonzaga 1998) aside from contamination change with time which is very predictable and was accounted for, and aside from the slowly decreasing charge transfer efficiency (Whitmore 1998). The scale and distortion of WFPC2 and NICMOS were taken into account in the calibration according to equations published by Trauger *et al*. (1995) and provided by STScI, causing corrections of up to 5% in a few cases.

Adopted Cross Sections

HST resolves the ring system into four groups. Integrated cross sections of ring particles were taken from Karkoschka (2001b) and are estimated to be accurate to 10% (Table III). They account for occultation and shadowing between ring particles which depend on subsolar latitude and phase angle. The resulting reflectivities are those of ring particles.

The adopted sizes of satellites (Table IV) are based on Davies *et al*. (1992) and Karkoschka (2001a). The minor satellites are assumed to be prolate spheroids with the tidally locked major axis a, which points toward Uranus, and the minor axis b in perpendicular directions. Their prolateness is $(a - b)/a$. With a baseline of a few years, HST may find evidence for true triaxial shapes such as those proposed theoretically by Thomas (1988). The apparent, elliptical disk has a short axis of b and a variable long axis of

$$a' = \sqrt{\{a^2 - (a^2 - b^2)[1 - (e/e_o)^2]\}}, \quad (1)$$

where e is the elongation from Uranus and e_o is the greatest elongation from Uranus, assuming a circular orbit.

For the purpose of presenting observed brightnesses and their uncertainties, the adopted cross sections are simply scale factors. When absolute reflectivities are interpreted physically, the uncertainties of cross sections need to be considered too. For a consistent comparison of observed brightnesses between different investigations, all previous reflectivities quoted here were adjusted to the cross sections adopted in this work.

Magnitudes at unit distance are calculated in this work via the equation

$$V = V_{sun} - 2.5 \log\{I/F(r/r_o)^2\}, \quad (2)$$

where $V_{sun} = -26.75$, I/F is the reflectivity, r = radius of object, and $r_o = 1$ AU.

TABLE IV
Satellite Sizes and Magnitudes

Satellite	$a \times b$ (km)	V_{max}	V_{min}	Δm (1°)	σ
Cordelia	25 × 18	10.81	11.00	0.09	0.35
Ophelia	27 × 19	10.45	10.64	0.09	0.25
Bianca	32 × 23	9.71	9.90	0.23	0.24
Cressida	46 × 37	8.80	8.93	0.23	0.11
Desdemona	45 × 27	9.15	9.40	0.23	0.16
Juliet	75 × 37	8.25	8.56	0.23	0.05
Portia	78 × 63	7.64	7.77	0.23	0.05
Rosalind	36	9.08	9.08	0.23	0.13
Belinda	64 × 32	8.60	8.92	0.23	0.09
S/1986 U 10	15	10.99	10.99	0.23	0.50
Puck	81	7.04	7.04	0.22	0.05
Miranda	240 × 234	3.07	3.09	0.41	0.04
Ariel	581 × 578	0.97	1.01	0.44	0.04
Umbriel	585	1.75	1.77	0.32	0.04
Titania	789	0.76	0.80	0.36	0.04
Oberon	761	0.98	1.00	0.36	0.04

Note. a, b are the adopted major and minor axis (radius); V_{max}, V_{min} are the maximum and minimum magnitude at 0° phase angle, at 1 AU from the sun and observer, and at a subsolar latitude of −40°; magnitudes from Earth at mean opposition distance are fainter by 12.71; Δm (1°) is the magnitude drop at 1° phase angle; σ is the uncertainty of magnitudes.

Error Estimation

All uncertainties in this work are 1-sigma error bars. Uncertainties were added via the square root of the sum of squares. The first contribution of the adopted uncertainty was the noise, estimated by placing the aperture at 12 positions 0.7″ from the satellite, every 30° in position angle. The second contribution was estimated by changing the aperture size by 20% in both directions. Finally, the 4% uncertainty of the reflectivity calibration was added. For the data on rings, an additional uncertainty was estimated from the closeness of other rings and/or Uranus. Larger error bars were applied to data in methane band filters (0.55, 0.62, 0.73, and 0.89 μm) because of suspected artifacts in their transmission curves such as a jump at 0.8 μm wavelength. Reflectivities with uncertainties near 0.1 or larger were discarded. Note that the selection was not based on the measured signal since such a selection yields positively biased values.

Voyager Data

This work uses only data from Voyager's clear filters with a mean wavelength of 0.48 μm since most objects do not have reliable data in other Voyager filters. Data for the major satellites were taken from Veverka *et al*. (1987), Helfenstein *et al*. (1988), and Skypeck *et al*. (1991). Data for the minor satellites come from Karkoschka (2001a). Data on the rings are based on Ockert *et al*. (1987) with an insignificant, positive 5% adjustment at low phase angles based on a reexamination of the

TABLE V
Reflectivities

Phase angle (°)	Wave length (μm)	Uranus	6, 5, 4 ring	α, β ring	η, γ, δ ring	ε ring	Bianca	Cress-ida	Desdemona	Juliet	Portia	Rosalind	Belinda	Puck	Miranda	Ariel	Umbriel	Titania	Oberon
0.034	0.34	515 ± 21	—	—	—	42 ± 16	—	—	—	—	—	—	—	109 ± 51	468 ± 21	476 ± 23	253 ± 12	308 ± 13	289 ± 12
	0.55	513 ± 21	—	—	—	52 ± 12	—	—	—	—	—	—	—	115 ± 53	449 ± 22	489 ± 21	251 ± 11	328 ± 14	309 ± 13
	0.63	458 ± 18	—	—	—	53 ± 16	—	—	—	—	—	—	—	134 ± 66	460 ± 26	497 ± 21	258 ± 11	339 ± 14	319 ± 13
	0.67	303 ± 12	—	—	—	50 ± 11	—	—	—	—	105 ± 69	—	—	104 ± 29	443 ± 19	502 ± 21	254 ± 11	350 ± 14	321 ± 13
	0.89	17 ± 1	—	—	62 ± 31	54 ± 10	—	—	—	—	—	—	—	—	434 ± 28	494 ± 31	f	f	353 ± 21
	0.91	50 ± 2	51 ± 23	59 ± 10	50 ± 8	51 ± 4	—	94 ± 30	66 ± 44	75 ± 21	86 ± 12	87 ± 37	63 ± 24	106 ± 8	428 ± 18	497 ± 20	253 ± 10	361 ± 15	s
0.079	1.08	120 ± 5	—	—	—	66 ± 28	—	—	—	—	—	—	—	—	f	f	f	f	f
	1.59	10.6 ± 0.4	64 ± 14	56 ± 6	56 ± 5	53 ± 3	89 ± 23	83 ± 15	90 ± 26	92 ± 9	82 ± 5	95 ± 24	78 ± 16	99 ± 6	f	430 ± 18	f	344 ± 16	f
	1.64	14.0 ± 0.6	63 ± 21	55 ± 12	56 ± 13	56 ± 7	—	—	—	132 ± 26	102 ± 18	—	89 ± 47	114 ± 9	f	f	f	f	f
	1.72	1.07 ± .04	64 ± 13	54 ± 6	55 ± 5	55 ± 3	—	53 ± 52	—	105 ± 30	101 ± 18	—	135 ± 39	108 ± 14	f	483 ± 20	f	387 ± 19	f
	1.87	0.83 ± .03	59 ± 12	56 ± 6	53 ± 5	55 ± 3	64 ± 68	74 ± 31	69 ± 40	98 ± 16	83 ± 9	63 ± 32	89 ± 20	105 ± 8	f	428 ± 17	f	347 ± 15	f
	2.03	0.31 ± .01	62 ± 15	56 ± 7	56 ± 6	56 ± 3	—	67 ± 55	—	96 ± 23	82 ± 14	—	88 ± 38	93 ± 11	f	270 ± 11	f	213 ± 10	f
0.081	1.59	10.6 ± 0.4	r	r	r	r	82 ± 55	72 ± 16	86 ± 35	87 ± 8	80 ± 9	91 ± 17	77 ± 11	101 ± 5	347 ± 14	f	f	f	f
	1.72	1.08 ± .04	r	r	r	r	—	60 ± 47	—	66 ± 26	101 ± 16	—	79 ± 39	98 ± 14	396 ± 18	f	f	f	f
	1.87	0.84 ± .03	r	r	r	r	100 ± 58	95 ± 31	99 ± 39	66 ± 15	83 ± 10	109 ± 37	84 ± 21	106 ± 8	351 ± 15	f	f	f	f
	2.03	0.32 ± .01	r	r	r	r	—	36 ± 51	—	71 ± 30	83 ± 16	—	90 ± 36	101 ± 12	228 ± 14	f	f	f	f
0.21	0.28	545 ± 22	—	—	—	—	—	—	—	—	—	—	—	—	—	382 ± 28	249 ± 25	286 ± 16	234 ± 11
	0.41	548 ± 22	—	—	—	42 ± 15	—	—	—	—	—	—	—	90 ± 54	380 ± 18	425 ± 21	232 ± 12	300 ± 12	246 ± 10
	0.54	328 ± 16	—	—	—	51 ± 29	—	—	—	—	—	—	—	—	377,32	404,21	220 ± 12	307 ± 15	f
	0.66	259 ± 10	—	—	—	48 ± 13	—	—	—	—	—	—	—	133 ± 59	374 ± 17	427 ± 18	229 ± 9	320 ± 13	282 ± 12
	0.87	73 ± 3	45 ± 25	47 ± 16	60 ± 11	50 ± 4	—	77 ± 34	78 ± 47	77 ± 16	71 ± 11	65 ± 43	92 ± 29	98 ± 9	369 ± 16	436 ± 18	234 ± 9	344 ± 14	s
	0.91	51 ± 2	40 ± 22	48 ± 9	55 ± 7	49 ± 4	-	55 ± 33	101 ± 43	91 ± 16	90 ± 10	41 ± 43	78 ± 26	91 ± 8	368 ± 17	438 ± 18	235 ± 10	342 ± 14	s
1.10	0.32	517 ± 21	—	—	—	43 ± 12	—	—	—	—	—	—	—	—	318 ± 18	336 ± 15	192 ± 8	227 ± 9	209 ± 9
	0.43	558 ± 22	—	—	—	44 ± 16	—	—	—	—	—	—	—	81 ± 57	331 ± 18	338 ± 15	193 ± 9	243 ± 10	216 ± 9
	0.62	133 ± 5	—	46 ± 30	30 ± 24	45 ± 8	—	—	—	—	36 ± 38	—	—	76 ± 17	313 ± 13	345 ± 14	189 ± 8	258 ± 10	231 ± 9
	0.73	46 ± 2	—	—	—	50 ± 9	—	—	—	—	—	—	—	—	290 ± 13	340 ± 14	186 ± 8	266 ± 11	237 ± 9
	0.79	118 ± 5	—	51 ± 20	28 ± 16	47 ± 5	—	51 ± 70	—	c	83,32	—	76 ± 39	91 ± 12	311 ± 14	352 ± 14	192 ± 8	267 ± 11	236 ± 10
	0.91	50 ± 2	51 ± 32	49 ± 18	48 ± 12	48 ± 5	—	24 ± 39	78 ± 41	c	80 ± 30	46 ± 35	61 ± 27	79 ± 8	312 ± 14	358 ± 14	197 ± 8	279 ± 11	242 ± 10
2.82	0.34	520 ± 21	—	—	—	38 ± 11	—	—	—	—	—	—	—	56 ± 55	297 ± 15	311 ± 15	157 ± 7	202 ± 9	171 ± 8
	0.47	591 ± 24	—	—	—	43 ± 13	—	—	—	—	—	—	—	—	280 ± 15	328 ± 16	158 ± 7	210 ± 9	186 ± 8
	0.59	540 ± 22	—	—	—	44 ± 17	—	—	—	—	—	—	—	98 ± 59	271 ± 13	328 ± 14	162 ± 7	220 ± 9	196 ± 8
	0.63	453 ± 18	—	—	—	43 ± 17	—	—	—	—	—	—	—	115 ± 70	268 ± 16	333 ± 15	162 ± 7	225 ± 9	197 ± 9
	0.87	s	46 ± 19	44 ± 10	43 ± 8	45 ± 4	—	53 ± 25	15 ± 37	c	70 ± 23	44 ± 24	17 ± 27	77 ± 5	278 ± 12	331 ± 14	170 ± 7	228 ± 9	209 ± 9
	0.91	50 ± 2	46 ± 29	48 ± 11	40 ± 10	43 ± 4	—	63 ± 35	71 ± 46	c	65 ± 24	37 ± 40	67 ± 38	71 ± 8	275 ± 13	334 ± 14	170 ± 7	241 ± 10	208 ± 9
	0.95	67 ± 3	—	—	—	42 ± 14	—	—	—	—	—	—	—	—	266 ± 19	340 ± 14	162 ± 7	246 ± 10	211 ± 9

Note. Listed are full-disk albedos and uncertainties of Uranus, ring particles, and satellites in units of 0.001. Symbols used are as follows: -, too faint, s, saturated, f, outside field of view; c, too close to Portia; r, ring measured in combined images of phase angles near 0.08°.

data. Data on the ε ring only were used in this work since other rings have low signals, typically 1 DN/pixel, causing systematic errors (Porco *et al*. 1987).

III. CLASSIFICATION OF OBJECTS

This section provides a rough look at the data while refined analysis is presented in the following sections. Table V lists all observational data. In Table VI, these data were averaged according to wavelength (0.73 to 0.95 μm and 1.59 to 2.03 μm) and according to phase angle (below and above 1°), normalized to Voyager's clear filter data at 16° phase angle (the normalization for the ε ring was used for the other rings). The seven innermost satellites listed in Table VI are called here the *Portia group*.

One can classify objects according to their photometric dependence with wavelength and phase angle, according to the three values of Table VI. Each pair of objects was compared with the chi-square test. For each of the 6 pairs between the 4 rings, and the 21 pairs within the Portia group, the test yields consistency. Thus, all ring particles can be represented by their average within the uncertainty of this work. The same is true for the members of the Portia group. This leaves 8 classes: ring particles, the Portia group, Puck, and the 5 major satellites. For 25 of the 28 pairs between these 8 classes, the test yields distinct, photometric variations. The 3 pairs between Umbriel, Titania, and Oberon seem to be consistent. However, their spectra shortward of 0.73 μm and their water ice absorption, discussed later, are very different from each other. Thus, there are 8 distinct surface classes within the uncertainty of the data.

An independent parameter for classification is the reflectivity (Table VI, first column after the name). The eight classes all have different reflectivities while there are no significant variations within each class. Note that some of the smaller satellites have uncertain reflectivities due to uncertain sizes (cf. Karkoschka 2001a).

Finally, one can classify objects positionally according to orbital radius. Each ring and each member of the Portia group has another object within 3% of the orbital radius while the orbital separation between the members of the eight classes is always more than 12%. Thus, there are three independent methods of classification: by photometric dependence with wavelength and phase angle, by reflectivity, and by orbital radius. All three methods yield the same classification.

The classification of ring particles is consistent with Karkoschka (1997) while Voyager data indicate a variation within the ring system (Ockert *et al*. 1987) which may possibly be caused by systematic effects at their low signal. The classification of the minor satellites is new. Previously, all minor satellites were considered similar since previous data did not show a significant difference between the Portia group and Puck.

TABLE VI
Averaged Reflectivities

Satellite, ring particles	$(I_{16}/F)_c$ (10^{-3}) $\alpha = 16°$ $\lambda = 0.48$ μm	$(I_\alpha/F)/(I_{16}/F)_c$ in % 1.8° 0.9 μm	0.08° 0.9 μm	0.08° 1.8 μm	σ (%)
6, 5, 4 ring	23:	213 ± 63	197 ± 59	269 ± 28	9
α, β ring	23:	210 ± 30	228 ± 28	240 ± 13	5
η, γ, δ ring	23:	185 ± 23	235 ± 21	238 ± 11	4
ε ring	23	202 ± 9	219 ± 10	238 ± 6	4
all rings	23	200 ± 8	222 ± 8	239 ± 5	4
Bianca	33	—	—	258 ± 56	22
Cressida	33	155 ± 55	240 ± 58	235 ± 28	10
Desdemona	33	154 ± 70	243 ± 77	255 ± 49	15
Juliet	33	—	251 ± 31	268 ± 14	5
Portia	33	224 ± 41	256 ± 20	255 ± 10	5
Rosalind	33	134 ± 55	206 ± 71	271 ± 36	12
Belinda	33	151 ± 47	228 ± 46	248 ± 21	8
Portia group	33	172 ± 23	248 ± 14	256 ± 7	4
Puck	47	170 ± 8	214 ± 11	219 ± 6	5
Miranda	210	138 ± 3	193 ± 5	151 ± 4	4
Ariel	240	144 ± 2	201 ± 4	150 ± 3	4
Umbriel	112	161 ± 3	222 ± 5	—	4
Titania	161	159 ± 3	224 ± 5	177 ± 4	4
Oberon	141	159 ± 3	237 ± 15	—	4

Note. σ is the uncertainty of combined HST data. A colon marks an assumed reflectivity.

IV. THE PHOTOMETRIC MODEL

The data of this work were used to constrain free parameters of a photometric model where the brightness is the product of four normalized functions and a constant: a lightcurve dependent only on orbital longitude, a phase function dependent only on phase angle, a continuum and absorption spectrum dependent only on wavelength, and the opposition brightness,

$$I/F(l, \alpha, \lambda) = f_1(l) f_2(\alpha) f_3(\lambda) f_4(\lambda) (I/F)_0, \qquad (3)$$

where l is the orbital longitude, α is the phase angle, λ is the wavelength, f_1 is the lightcurve with an orbital average of unity, f_2 is the phase law scaled to unity at $\alpha = 0$, f_3 is the continuum spectrum scaled to unity at 550 nm, f_4 is the band/continuum ratio, and $(I/F)_0$ is the reflectivity at $\alpha = 0, \lambda = 0.55$ μm, longitudinally averaged. The lightcurves of major satellites were based on their shapes and albedo features measured by Voyager. The lightcurves of minor satellites were consistent with no albedo features but with the satellite's prolateness as a free parameter. The adopted phase functions had two parameters: the phase coefficient was based on Voyager photometry while the opposition surge dependence had a free parameter. The continuum spectra had the spectral slope as a free parameter. The absorption spectrum of water ice was modeled with an assumed shape and its depth as a free parameter. The opposition magnitude in the visible was a free parameter.

The free parameters were fitted to the data via least-square iteration which converged rapidly. The 315 data points on the

TABLE VII
Parameters of the Photometric Model

Object	I_0/F (10^{-3})	I_1/F (10^{-3})	α_o (°)	β (mag/°)	γ	f_{ice}	β_o (mag/°)	q (10^{-2})	qI_0/F (10^{-3})	ϖ	$S(O)$	h
Ring particles	50	46	8	0.030	0.09	1.00	0.1	36 ± 6	18 ± 3	0.06	0.25	0.06
Portia group	80	65	1.5	0.030	0.09	0.93	0.4	33 ± 8	26 ± 5	0.09	0.34	0.05
Puck	104	85	1.5	0.025	0.04	0.91	0.4	34 ± 6	35 ± 6	0.14	0.37	0.04
Miranda	464	318	0.3	0.024	−0.05	0.56	1.7	44 ± 7	200 ± 30	0.58	1.00	0.025
Ariel	533	355	0.2	0.025	0.07	0.52	2.5	43 ± 5	230 ± 25	0.64	1.00	0.025
Umbriel	258	192	0.7	0.027	0.02	0.76	0.7	39 ± 4	100 ± 10	0.33	0.80	0.035
Titania	350	252	0.5	0.023	0.18	0.51	1.0	46 ± 5	170 ± 15	0.49	0.75	0.025
Oberon	309	222	0.5	0.023	0.15	0.57	1.0	44 ± 5	140 ± 15	0.43	0.75	0.025

Note. Symbols used are as follows: I_0/F, I_1/F, reflectivities (V) at 0 and 1° phase angle; α_o, width of the opposition surge, cf. Eq. (4); β, phase coefficient; γ, spectrophotometric gradient; f_{ice}, band/continuum ratio at 2 μm wavelength; β_o, opposition phase coefficient; q, phase integral; qI_0/F, bond albedo. Hapke parameters ϖ, $S(O)$, h, $g = -0.28$, $\theta = 23°$, $B_{co} = 4$, and $h_c = 0.001$ are explained in the text.

rings and satellites of this work constrain 40 free parameters (cf. Table VII), a well-constrained problem. Various sophistications of the photometric model were tested, as discussed in this work, but none was found significant.

The photometric model can be used to predict the brightness for various observing conditions, subsolar latitude, orbital longitude, phase angle, and wavelength. For conditions well within the observed range, they are expected to be accurate to the uncertainties listed in Table VI and to about twice that value near the limits of the observed ranges, except that the water ice absorption is only constrained at the filter passbands. This model also fits most photometric Voyager data.

V. ROTATIONAL LIGHTCURVES

For the major satellites, Veverka *et al*. (1991) measured the variation of albedo with longitude in Voyager images. Assuming that the albedo is constant along each meridian, the rotational lightcurves were calculated for the subsolar latitude of the HST images (−40°). These lightcurves have peak-to-peak amplitudes around 0.03 magnitude or 3% as displayed in Fig. 4. Observed reflectivities were thus reduced to rotationally averaged reflectivities, presented in the following sections.

A Fourier analysis of these lightcurves revealed that amplitudes of twice the orbital frequency are already an order of magnitude smaller than those of the orbital frequency. Thus, these lightcurves are essentially sine curves, which is evident in Fig. 4. This is expected for viewing from high latitudes but not for near-equatorial viewing (cf. Pluto, Tholen and Buie 1997).

Nonspherical shapes of satellites in synchronous rotation cause lightcurves with twice the orbital frequency. Maxima occur at greatest elongation since the satellite's long axis is expected to point at the planet. Thus, periodicity and phasing of lightcurves give evidence for albedo features and satellite shape. Since Voyager data did not constrain lightcurves of minor satellites, they were estimated here by fitting the dependence

$$\text{brightness} \sim 1 + C_1 \cos(l - l_o) - C_2 \cos(2l) \qquad (4)$$

to the data of this work with variations due to phase angle and wavelength taken into account. The free parameters are C_1, C_2, and l_o while l is the subsolar longitude. The cosine terms in Eq. (4) account for albedo features and for satellite shape, respectively.

On Puck and throughout the Portia group, no significant albedo feature was detectable (Fig. 4, solid curves), and this was adopted here. Albedo features on individual members of the Portia group could be somewhat larger than on the major satellites, but far below that of Iapetus which has a 1.8 magnitude amplitude, about 50 times larger than that of the major satellites.

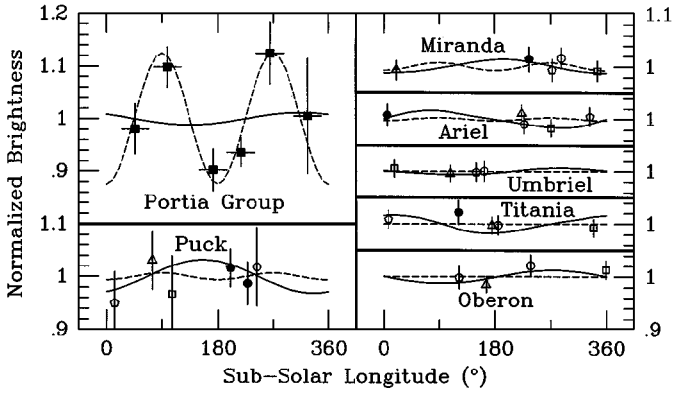

FIG. 4. Normalized brightness as a function of subsolar longitude due to surface albedo features (solid curves, 360° period) and satellite shape (dashed curves, 180° period). The curves for the major satellites (right) are based on published Voyager data while the curves for the minor satellites (left) are fitted to the data of this work. Puck's curves and the Portia group's solid curve have insignificant amplitudes (less than one sigma which is the expected noise). The Portia group's dashed curve has an amplitude of four sigma. The symbols have the same meaning as in Fig. 5. For the Portia group the symbols represent averages of all data points within each 60° interval.

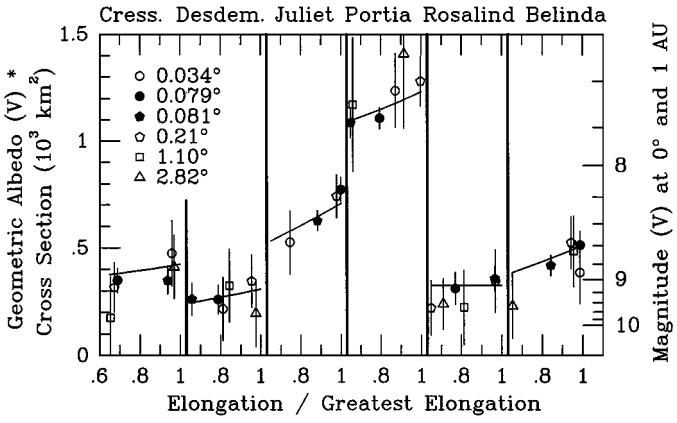

FIG. 5. Opposition brightness in the visible of the minor satellites as a function of their apparent relative elongation from Uranus. Plotted are data corrected for phase function and spectral dependence (Sections VI and VII). Open and solid symbols derive from observations at wavelengths near 0.9 and 1.8 μm, respectively. Most satellites display a positive correlation between relative elongation and brightness indicating a nonspherical shape. The curves displayed are calculated with the adopted albedos and shapes.

Puck's weak variation with twice the orbital frequency corresponds to a prolateness of 0.02 ± 0.09, consistent with the resolved imaging value of 0.03 ± 0.04 by Karkoschka (2001a). This is consistent with spherical shape which was adopted here. On the other hand, the Portia group has a very strong signal at twice the orbital frequency (Fig. 4, dashed curve), allowing the determination of each member's shape.

The most important constraints on satellite shape come from both NICMOS observations (solid symbols in Fig. 5) which have essentially identical phase angle and wavelength but orbital positions changed by about 50 degrees. The symbols in Fig. 5 indicate that correlations between elongation and phase angle or wavelength are sufficiently small to allow the determination of shape independently of the phase function and spectrum.

A least-square analysis gives a prolateness of 0.2 ± 0.15 for Portia and a lower limit of 0.4 for Juliet and Belinda. Cressida, Desdemona, and Rosalind also show positive correlations between elongation and brightness, evidence of a prolate shape. These shapes are very consistent with the shapes determined from resolved imaging (cf. Karkoschka 2001a).

VI. PHASE FUNCTIONS

Opposition Surge

All WFPC2 data on each date were averaged after correcting for the spectral slope. The wavelength of 0.55 μm served as the standard since many previous investigations provided data at or near that wavelength. Because the spectra of the uranian satellites are not very steep, the spectral correction was usually very small. For example, albedos vary only by about 1% between the Voyager clear filter (0.48 μm) and 0.55 μm. Figure 6 displays the phase functions. The HST and Voyager data complement each other.

The observed opposition surges were initially fitted with many functions, published ones and others. The best fits with the fewest free parameters were obtained for the adopted function where the opposition surge is the inverse of a linear function of phase angle with initially two free parameters, β and γ. Fixing γ at 0.5 magnitude still provided good fits. This yielded phase functions of the form

$$\Delta m(\alpha) = \beta\alpha + 0.5\alpha/(\alpha_o + \alpha), \quad (5)$$

where Δm is the magnitude difference between opposition and phase angle α. The first term on the right side is the standard linear dependence with a phase coefficient of β. The other term is the opposition surge dependence. Its width at half maximum is α_o. Its size depends somewhat on its definition and varies between zero ($\alpha_o \to \infty$) and 0.5 mag ($\alpha_o \to 0$). For example, Gehrels and Tedesco (1979) defined the size of the opposition surge as the difference between the linear extrapolation from 7° to 0° and the actual magnitude at 0°. This definition gives opposition surges near 0.1 (ring particles), 0.3 (minor satellites), and 0.5 mag (major satellites).

Voyager data are sensitive to the choice of the phase coefficient β, but not to the width of the opposition surge α_o. On the other hand, HST data are sensitive to α_o but hardly to β. Therefore, the listed values of β in Table VII are almost identical to Voyager-based values (Veverka *et al*. 1987, Thomas *et al*. 1989) while the values of α_o give important new information. Figure 6 shows that Voyager and HST data are well fitted by the adopted phase curves. This does not apply to Voyager data beyond 100° phase angle where simple functions such as Eq. (5) fit poorly.

Fitting Voyager and HST data with the same phase curves assumes that there are no major north–south asymmetries in albedo, given that the subsolar latitude moved north by some 40° between the times of the observations. Pluto, for example, darkened by 0.2 mag for the same shift of subsolar latitude (Tholen and Buie 1997). The agreement of the two data sets for Titania at some phase angles rules out a significant north–south asymmetry. Phase curves of the other major satellites cannot be fit as well if one adds an offset between Voyager and HST data of 0.05 mag. Therefore, latitudinal albedo variations are probably comparable in size to longitudinal albedo variations where a shift of subsolar longitude of 40° causes changes of 0.01–0.02 mag (cf. Fig. 4). Such shifts between Voyager and HST data would not significantly change the parameters of the phase curves.

Goguen *et al*. (1989) observed Titania and Oberon in the visible and fitted their data with the simple linear dependence of magnitude versus phase angle. Most of their observations (16 out of 17) occurred between 0.5 and 3° phase angle. Their average levels in this interval agree to 1% with those of this work. They questioned whether their data points at 0.06° phase angle were valid because of poor observing conditions on that date, and because both data points plotted 0.2 mag above their linear fits. However, the new phase functions are indeed 0.2 mag above

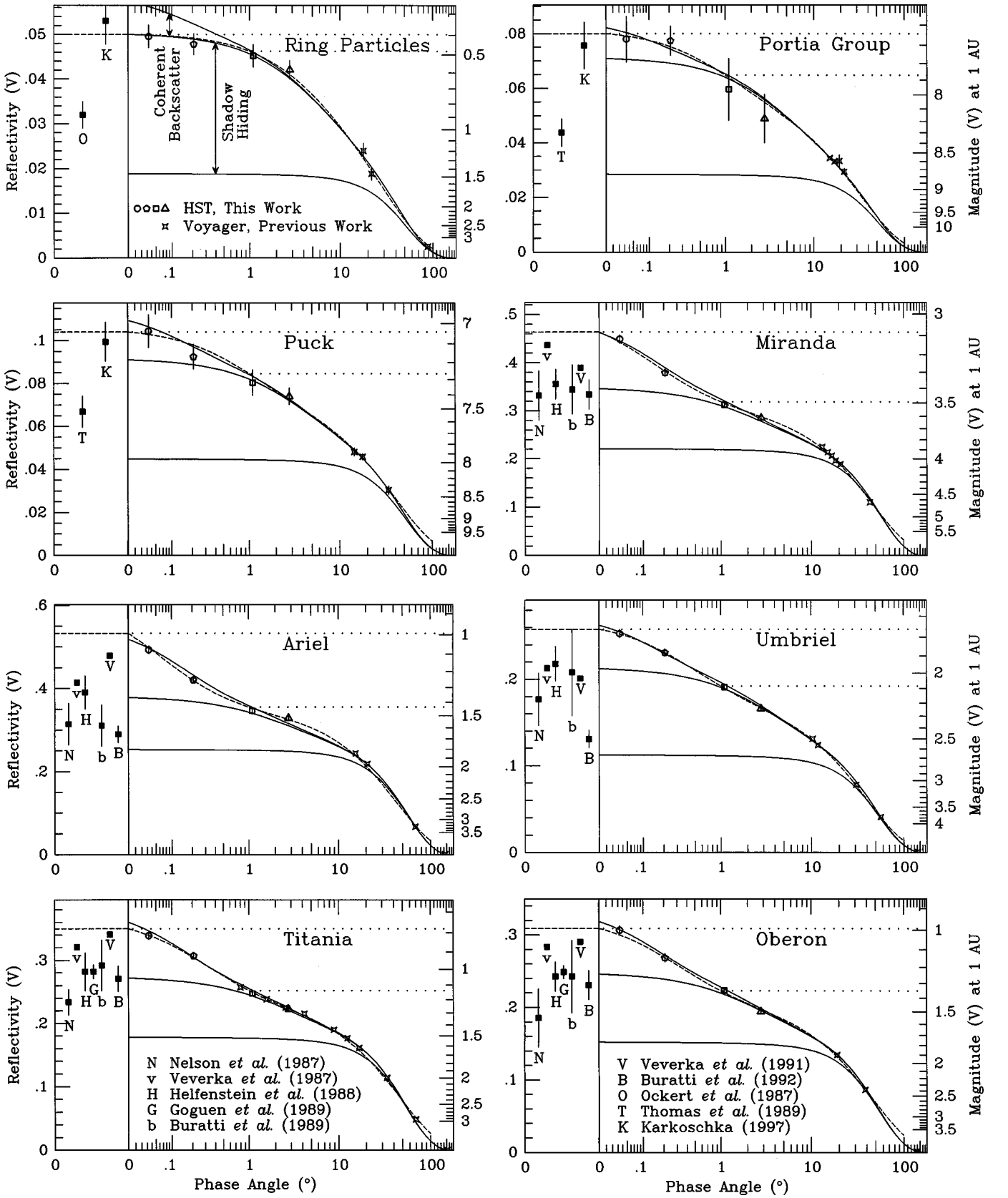

FIG. 6. Phase functions in the visible based on the data in this work (open symbols) and previoulsy published Voyager data (stars). The dashed lines are the nominal fits of this work (cf. Eq. (5), Table VII). The left panels show previous estimates of the geometric albedo. Solid curves are Hapke phase functions with coherent backscatter (top curve), without coherent backscatter (middle curve), and without shadow hiding opposition surge (bottom curve, cf. Table VII for the adopted parameters). The magnitude scale for ring particles refers to the combined cross section of all ring particles of 1.95×10^7 km^2 (cf. Table III). The magnitude scale for the Portia group refers to Portia at greatest elongation and can be adjusted for the other members according to data listed in Table IV. The phase angle scale is logarithmic in $\alpha + 0.05^\circ$ which is almost logarithmic but allows the inclusion of $\alpha = 0^\circ$ (α is the phase angle).

their linear functions at 0.06° phase angle, indicating that their observations were good.

Phase curves of four satellites in the visible by Buratti *et al*. (1992) are half a magnitude fainter than those of this work, probably a calibration issue. The two data sets agree roughly about the shape of the phase curves for Titania and Oberon, but not at all for Ariel and Umbriel, possibly due to difficulties of ground-based photometry in the visible so close to Uranus.

Brown and Cruikshank (1983) concluded that Ariel, Titania, and Oberon have large opposition surges based on near-infrared photometry. While they do not give an absolute calibration nor error bars, the shapes of their phase curves agree with those of this work except for one data point of Titania which seemed to indicate a much larger opposition surge.

Near-infrared observations by Baines *et al*. (1998) indicated that Miranda's phase curve has a slope of 1.5 ± 1.0 mag/° between 0.6 and 1.0° phase angle in the K-band, much larger than that of the other major satellites. On the other hand, this work indicates that Miranda's slope in the visible is 0.15 ± 0.05 mag/° between 0.6 and 1.0°, comparable to that of the other satellites. The difference is hardly significant considering uncertainties. Their slope in the H-band data agrees still better with the slope of this work.

Herbst *et al*. (1987) measured the ring's phase function in the near-infrared which is quite consistent with the ring's phase function observed at shorter wavelengths in this work.

The slope of the phase curve, the differentiation of Eq. (5) is

$$\mathrm{dm}(\alpha)/\mathrm{d}\alpha = \beta + 0.5\alpha_o/(\alpha_o + \alpha)^2. \quad (6)$$

The slope at 0° phase angle, $\beta_o = \beta + 0.5/\alpha_o$, is listed in Table VII. It is probably larger than 2 mag/° for Ariel. On the other hand, no variation with phase angle was detectable for Uranus which puts an upper limit of 0.003 mag/° on β_o, consistent with the more accurate determination by Lockwood and Thompson (1999, near 0.002 mag/°). Thus, there is a factor of 1000 variation of β_o within the uranian system. Ariel and Uranus may be the objects in the solar system with the largest and smallest β_o in the visible. Note that the slope of Ariel's phase curve varies by a factor of 100 between 0° and moderate phase angles which cannot be displayed well in common plots with a linear phase angle scale. On the other hand, the variations of magnitude between 0.03° and 0.3° and between 0.3° and 3° are similar, favoring near-logarithmic phase angle scales such as those in Fig. 6.

Geometric Albedos

A selection of published geometric albedos are shown in Fig. 6 to the left of the vertical line for each object (filled squares). Almost all these previous numbers are well below the new data at 0.03° phase angle, typically by a factor of 1.3 and by as much as a factor of 2. With respect to geometric albedos and opposition magnitudes, which are probably the most commonly published photometric quantities, the uranian ring and satellite system is significantly brighter than currently believed. While there is good agreement with most previous data concerning reflectivities above 1° phase angle, most previous investigations lacked data at lower phase angles and used various techniques of extrapolation.

Unless data are presented at phase angles well below 1°, the common practice of extrapolating phase curves to 0° seems questionable. The reliability of extrapolation is hard to estimate, which caused many unrealistic error bars. Perhaps future investigators will compare reflectivities and magnitudes at a standard phase angle such as 1°, at which they are far better constrained by most data sets. All outer planets and their systems can regularly be observed at 1° phase angle, but rarely close to 0°. Magnitudes and reflectivies at 1° phase angle are listed in Tables V and VII.

Some of the uranian satellites seem to have exceptionally steep opposition surges. This perception may actually be a result of the unusually dense low-phase-angle sampling of the uranian system achieved in our work. When examined at extremely low phase angles, other bodies also seem to exhibit steep opposition surges. Helfenstein *et al*. (1998) investigated Galileo images of Europa and found regions with very steep phase functions shortward of 0.2° phase angle where no previous observation existed. The slope of the phase curve for icy terrains on Europa was similar to Ariel's and much larger still for one dark spot on Europa. Once more objects have been observed at such low phase angles, the steep opposition surges of uranian satellites may be found to be more common.

Phase Integrals

The adopted nominal phase functions were integrated to provide the bond albedo. For this integration, the reflectivity was somewhat decreased above 70° phase angle to account for the fact that near or above 70°, phase functions tend to become steeper. This correction is not critical since ~80% of the reflected light is reflected toward angles below 70°. Table VII lists the resulting bond albedos in the visible. Since only 5–10% of the reflected light is reflected toward angles less than 15° (typically the lowest angle of Voyager data), bond albedos are almost entirely determined by Voyager data alone. Not surprisingly, the values listed here agree quite well with previous bond albedos based on Voyager data (Nelson *et al*. 1987, Veverka *et al*. 1987, Helfenstein *et al*. 1988, Buratti *et al*. 1990). Dividing bond albedos by the geometric albedos yields the phase integrals, also listed in Table VII. The derived values are almost always smaller than previously reported which comes from previous underestimation of geometric albedos.

VII. SPECTRAL SLOPES

The albedo spectra of uranian rings and satellites are quite flat. Voyager found all rings, minor satellites, and major satellites to be gray within error bars, with the exception of Titania's positive, barely significant spectral slope. By using a wider spectral range, Karkoschka (1997) found that the rings and satellites

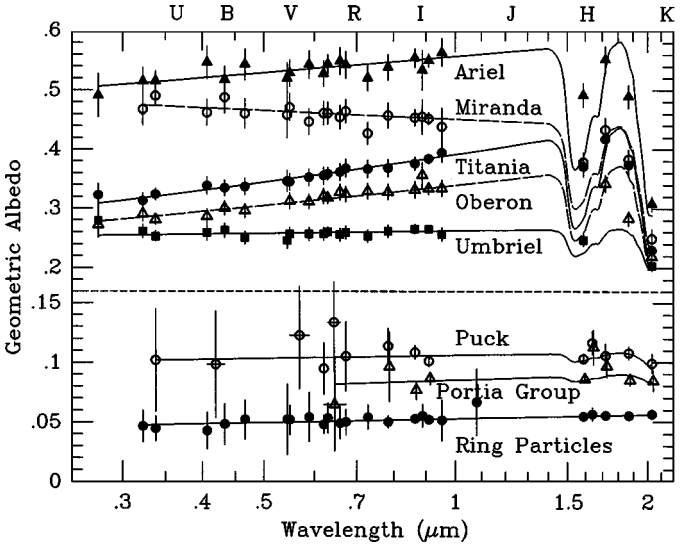

FIG. 7. Observed geometric albedo spectral data of this work and their fitted spectra, which are featureless aside from the water ice absorption in the near-infrared. The centers of standard photometric bands are indicated at the top. Note the change of vertical scale at the dashed line.

have various distinct spectral slopes. With the phase functions of Section VI, all data of this work were reduced to 0° phase angle (Fig. 7).

Spectral data were fitted by least-square power laws (Fig. 7). Data points with significant water ice absorption beyond 1.4 μm wavelength were excluded from the fit. The adopted continuum spectra are

$$I_o/F(\lambda) = I_o/F(\lambda_o)(\lambda/\lambda_o)^{\gamma} \quad (7)$$

with the spectrophotometric gradients γ and $I_o/F(0.55\ \mu\text{m})$ listed in Table VII. Uniquely related to γ are color indices (Table VIII).

Spectrophotometric gradients were also given in Fig. 3 of Karkoschka (1997) for 10 objects, consistent with those of this work for 9 objects. The ε ring's spectrum is probably somewhat shallower than the previous determination since the new investigation has larger spectral regions and thus smaller uncertainties for spectrophotometric gradients, 0.03 for the major satellites, 0.06 for the rings and Puck, and 0.09 for the Portia group.

Baines *et al*. (1998) extended the data set of Karkoschka (1997) with near-infrared photometry. The flatness of their ring spectrum is very consistent with Nicholson *et al*. (1982) and with this work. However, their observations are consistently 30% brighter than those in this work. Their data of ring ansae are 20% brighter than expected from this work, taking into account the longitudinal brightness variation (Karkoschka 2001b). Baines *et al*. (1998) noted spectral differences between Miranda, Ariel, and Titania, somewhat similar to the results of this work, although an accurate comparison would require the shape of satellite spectra and filter curves.

TABLE VIII
Color Indices

Object	U–V	B–V	V–R	V–I	V–J	V–H	V–K
Rings	0.88	0.67	0.55	0.88	1.20	1.54	1.63
Portia group	—	—	0.55	0.88	1.20	1.51	1.59
Puck	0.86:	0.66:	0.54	0.85	1.15	1.43	1.50
Miranda	0.82	0.64	0.52	0.80	1.08	1.14:	1.16:
Ariel	0.87	0.66	0.55	0.87	1.18	1.25:	1.30:
Umbriel	0.85	0.66	0.54	0.84	1.14	1.35:	1.40:
Titania	0.92	0.69	0.57	0.92	1.28	1.38:	1.46:
Oberon	0.91	0.69	0.57	0.91	1.25	1.38:	1.46:
Sun, assumed	0.84	0.65	0.53	0.83	1.12	1.43	1.49

Note. Aside from the uncertainty of the solar values, color indices are accurate to about 0.02 except for values marked by a colon where the uncertainty is 0.1.

Comparison with Voyager Data

Voyager provided important spectral information for the major satellites, summarized by Nelson *et al*. (1987) for two filters of the photopolarimeter (PPS) and by Buratti *et al*. (1990) for five filters of the imaging cameras (ISS). In order to scale their geometric albedos to the spectral fits of this work, they need a satellite-dependent increase between 35% (Titania) and 65% (Ariel) and a filter-dependent increase of 12% and 7% (ultraviolet and infrared of PPS) and −2, 4, 0, 1, and 1% (ultraviolet, violet, clear, green, and orange of ISS). The former, large discrepancy has been discussed in Section VI while the latter variation can be interpreted as filter calibration offsets which are consistent with quoted uncertainties of 10% absolute and 4% within each camera.

There is no indication of any other systematic effects. The remaining scatter (rms) of these 35 data points is 5%, which is well below quoted uncertainties. The same is true for the 2% scatter of the 91 data points of this work for the major satellites shortward of 1 μm.

VIII. WATER ICE ABSORPTION

Water has strong absorption bands near 1.6 and 2 μm wavelength which have been identified in the spectra of many satellites, including the major uranian satellites. This work presents the first such observations of the minor satellites. For the major satellites, the near-infrared data of this work were also analyzed, but the spectral coverage of Brown and Cruikshank (1983) and Roush *et al*. (1998) is superior.

Each wide NICMOS filter used in this study probes an average across a significant part of a water ice absorption band. The data were interpreted with a crude model where the band/continuum ratio of each spectrum is the band/continuum ratio of a reference spectrum raised to a certain power. The exponent was a free parameter for a least-square fit to the data. The reference spectrum was that of the leading side of Rhea (Clark *et al*. 1984) because of its low noise and high spectral resolution, with a linear fit to its

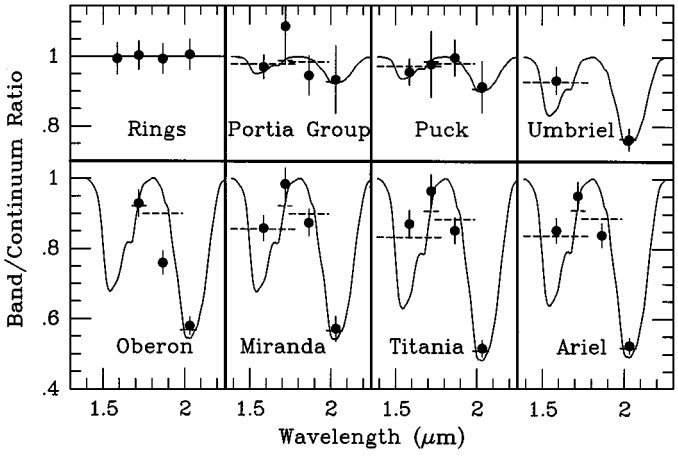

FIG. 8. Spectral data (solid dots) near the water ice absorption normalized by the linear spectral fits. The solid curves show Rhea's spectrum scaled to match the observed absorption depth at 2.03 μm wavelength. Convolving those spectra with the filter bandpasses yields the expected levels indicated by the dashed lines. The width of each dashed line indicates the bandpass of the filter. The objects are ordered here according to increasing geometric albedo at the continuum near 2 μm wavelength which seemingly coincides with increasing water ice absorption.

maxima defining the continuum. Model spectra were convolved with the filter curves for a comparison with the data (Fig. 8).

Most data points are consistent with the adopted spectral shapes, although the data at 1.72 and 1.87 μm are systematically high and low, respectively. Recent preliminary spectra with better spectral resolution by Roush *et al*. (1998) also revealed anomalous spectral shapes. The brightest surfaces have the strongest absorptions, which Brown and Cruikshank (1983) already noted for the four largest satellites. The same correlation is observed in mixtures of rocky and icy surface material varying from deep absorptions for bright surfaces to minuscule absorptions for dark surfaces (Clark and Lucey 1984).

The Portia group and Puck show a small dip at 2.03 μm wavelength. The statistical method of variances for all data yields a spectral absorption for the Portia group well below 1 sigma, the uncertainty, while for Puck it is 1.5 sigma. The latter is a marginal detection of water ice.

The near-infrared ring spectrum is perfectly flat with high precision. This result supports the assertion that Puck's absorption feature is not due to filter calibration offsets. The flat, infrared ring spectrum of Baines *et al*. (1998) was more sensitive to hydrocarbon ice absorption while the 2.03 μm filter of this work is more sensitive to water ice absorption.

IX. HAPKE PHASE FUNCTIONS

A physically more meaningful fit of phase functions than that of Eq. (5) was introduced by Hapke (1984). The phase function is dependent on five parameters: the single scattering albedo of grains near the surface ϖ, their asymmetry parameter g, the macroscopic mean slope of the surface θ, and two parameters for the size and width of the shadow-hiding opposition surge, S(O) and h. Since the shape of the single scattering phase function is not well constrained by observations, it is assumed to be a Henyey–Greenstein function according to common practice. Hapke (1998) included the coherent backscattering peak by multiplying the multiple scattering term of the five-parameter function by $1 + B_{co}\,(1 - e^{-f(\alpha)})/f(\alpha)$ with $f(\alpha) = (\tan\alpha/2)/h_c$. The parameters B_{co} and h_c define the amplitude and width of the coherent backscattering peak. This approach is adopted here as a possible explanation of the observed opposition surges. Theoretical analysis of the opposition surge is in progress and may yield alternate explanations.

Unfortunately, different combinations of parameters of the five-parameter model can yield almost identical phase curves, making a fit very sensitive to observational errors. For example, a small revision of a single data point caused Ariel's fitted surface roughness (θ) to change from $42 \pm 10^\circ$ (Helfenstein *et al*. 1988) to $27 \pm 1^\circ$ (Skypeck *et al*. 1991). The situation is worse for a seven-parameter fit. Therefore, the goal of this section is *not* to provide a best fit, but to reduce the number of free parameters enough that variations in the derived quantities may yield some physical insight. Emphasis was put on small phase angles because of the data of this work.

The parameters g and θ have little influence on the shape of the phase curve at small phase angles. They were fixed at -0.28 and 23°, respectively, based on previous investigations of the major satellites (Helfenstein *et al*. 1988, Buratti *et al*. 1990, Skypeck *et al*. 1991). The parameter h_c fixed at 0.001 worked for every phase curve, but twice or half that value could be excluded in some cases. This means that the coherent backscatter has a width at half maximum of slightly larger than 0.1°.

Helfenstein *et al*. (1988) gave a five-parameter fit for Titania based on Voyager data (minumum phase angle 0.8°). The new data demonstrate that the actual phase function shortward of 0.8° is much steeper than according to this fit. This difference can be explained by coherent backscatter with a parameter $B_{co} = 4$. The same value was also adopted for all other satellites. It is not well constrained by observations since somewhat larger or smaller values of B_{co} also fit the data if S(O) is adjusted the opposite way.

This leaves three adjustable parameters for each object. The single scattering albedo ϖ is well constrained by Voyager data above 20° phase angle where the contribution from the opposition surge is small. The opposition surge parameters S(O) and h are well constrained by the new data. The best fitting parameters are listed in Table VII, but no error bars are listed since a search of the seven-dimensional parameter space was not done.

The resulting phase curves are shown in Fig. 6 as the top solid lines. Setting the coherent backscatter B_{co} to zero leaves the five-parameter fit, displayed as the central solid lines. These fits are perfectly consistent with all Voyager data but are not consistent with the new data near 0° phase angle. For the major satellites, they are comparable to previous Hapke phase functions. While previous opposition surge parameters have mostly been assumed

to be identical due to lack of data, the new data require different values between objects. The phase function of ring particles is better fitted with a smaller coherent backscatter peak (B_{co}) or none at all. The bottom curves of Fig. 6 give Hapke functions with the shadow-hiding opposition surge S(O) set to zero in order to show the importance of this parameter.

Hapke functions of Ariel, Titania, and Oberon fit very well but Miranda's and Umbriel's residuals could be reduced by scaling the Voyager data a few percent down with respect to the HST data. This would mean that the albedo has been decreasing since 1986 and that the northern hemispheres of Miranda and Umbriel are generally darker than the southern hemispheres imaged by Voyager. Such a claim may be made in a few years as more of the northern hemispheres become visible.

Correlations

Correlations between the Hapke parameters found in this work are shown in Fig. 9. With increasing single scattering albedo, the size parameter for the shadow-hiding opposition surge increases by a factor of 4 while its width parameter decreases by a factor of 2. These correlations originate from correlations between surface albedos and the shapes of phase curves. Objects with the darkest surfaces have the steepest slopes between 1° and 16° phase angle (Fig. 10). Similar correlations have been seen in many parts of the solar system, even among surface albedo features, although not always such a close correlation. On the other hand, the variation between 0° and 1° has the opposite correlation (cf. Fig. 10) which may seem unexpected.

Coherent backscatter is a phenomenon of multiply scattered light and thus most significant for bright surfaces. On the other hand, shadow hiding is a phenomenon of single scattered light and thus most significant for dark surfaces. Therefore, one expects that coherent backscatter is large for bright surfaces while shadow hiding is large for dark surfaces. The observed phase functions (Fig. 6) confirm that this is indeed the case. Since coherent backscatter operates close to phase angle 0°, the reflectivity varies strongly between 0 and 1° phase angle for bright surfaces. Since shadow hiding varies mostly typically between 1 and 16° phase angle, the reflectivity varies strongly between those phase angles for dark surfaces.

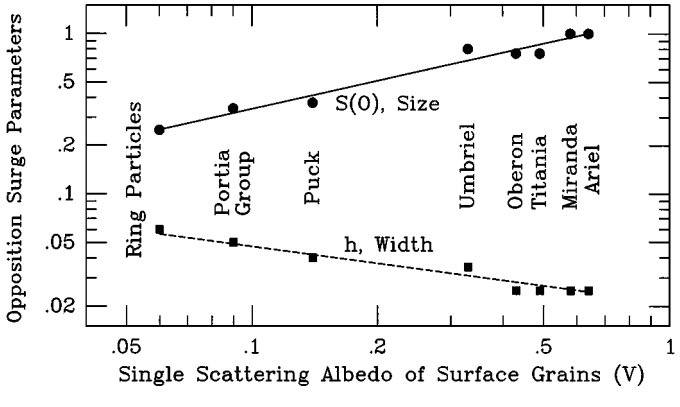

FIG. 9. Correlations between the single scattering albedo and the opposition surge parameters of the Hapke phase functions.

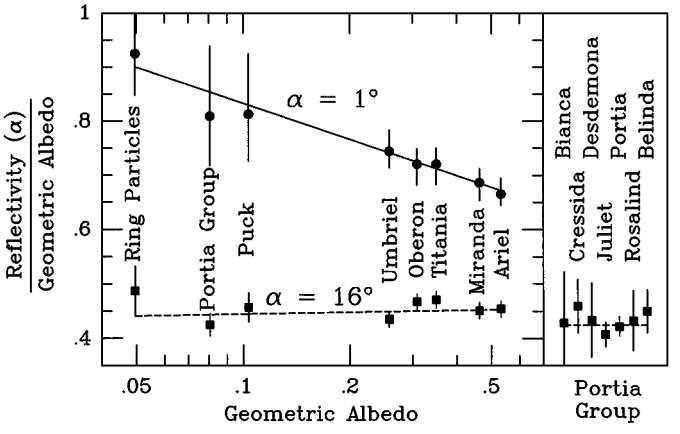

FIG. 10. Normalized reflectivities at 1 and 16° phase angles. These data are strongly correlated with the geometric albedo. The brightest surfaces have the strongest variation of reflectivity with phase angle between 0 and 1° and the smallest variation between 1 and 16°. Data for each member of the Portia group are consistent with their average (right panel).

The uranian system seems to be simple. With the knowledge of one brightness parameter such as geometric albedo or single scattering albedo, one can predict many other parameters based on strong correlations.

All data points of Fig. 10 are consistent with the indicated correlations except the 16° data for Titania and Oberon which are slightly above the fit. On the other hand, spectral slopes in the uranian system are very shallow with the exception of Titania and Oberon which show steeper slopes. These two deviations could be related, e.g., a yellow surface "ingredient" with a relatively shallow phase function, which is more abundant on Titania and Oberon than on other surfaces. Both deviations seem to be observationally significant, but a causal connection is pure speculation at this point.

Wavelength Dependence

For the major satellites, the uncertainty of the data is typically an order of magnitude smaller than the size of observed variations with wavelength and phase angle. Thus, these data can test the assumption of the photometric model that variations with wavelength and phase angle are independent. For the major satellites, the three filters including data at the smallest and largest sampled phase angle (0.34, 0.63, and 0.91 μm) show no evidence of a variation of the phase curve with wavelength. The same conclusion is reached when other filters and intermediate phase angles are considered.

Assuming that all Hapke parameters but the single scattering albedo are wavelength independent, the observed geometric albedo spectra were transformed into spectra of the single scattering albedo (Fig. 11). With this assumption, the dependence of Hapke phase functions on wavelength was calculated for the

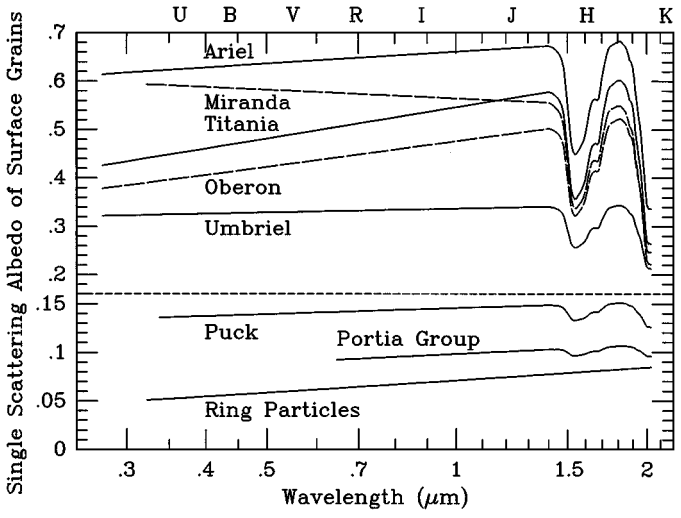

FIG. 11. Single scattering albedo as a function of wavelength if the other Hapke parameters are assumed wavelength independent. The spectral shape of the water ice absorption is based on the curves of Fig. 8.

observed objects. The normalized, theoretical phase functions do only slightly depend on wavelength below 3° phase angle, by less than 1%, much less than observational uncertainties, which is consistent with the photometric model. Thus, phase curves of uranian objects from all Earth-based observations can probably be considered wavelength independent, at least at continuum wavelengths.

At higher phase angles, theoretical phase curves steepen slightly towards shorter wavelengths. There is a hint of this in the steep spectra of Titania and Oberon observed with the wide spectral range of the PPS camera. It was already noticed by Buratti *et al*. (1990). Phase integrals are expected to be minimally wavelength dependent. Bond albedo spectra are expected to be slightly steeper than geometric albedo spectra.

The width of the coherent backscatter (h_c) increases with wavelength according to theoretical considerations (Mishchenko 1992). An observational confirmation would require a better sampling of the phase curve below 0.2° than provided in this work.

X. FAINT SATELLITES

Current longitudes of the minor satellites discussed in the previous sections are known to about 0.1° based on their recovery in 1994 HST images (Jacobson 1998). On the other hand, the three faintest regular satellites of Uranus, Cordelia, Ophelia, and S/1986 U 10 were not detected by HST and have no accurate prediction since they were only imaged for 1–2 weeks in 1986. For example, orbital elements by Owen and Synnott (1987) and by Jacobson (1998) yield uncertainties of Ophelia's longitude in July, 1997 of ±157 and ±38°, respectively, based on the same Voyager data. The uncertainty according to French and Nicholson (1995) based on Ophelia's gravity on a wave in the outer edge of the ε ring is only ±4°, but this determination was less reliable since the wave was barely detectable.

Because of uncertain predictions, aperture photometry was performed for each possible orbital motion. Due to Cordelia's and Ophelia's closeness to the bright, nearby ε ring, their sky brightness was taken from a region behind and ahead in their orbits. In order to build up signal, the photometry of all images with significant signals (cf. Table II) was added with weights according to the expected signal-to-noise ratio (Fig. 12).

Ophelia is clearly visible near the position predicted by French and Nicholson (1995) and some 45° ahead of and behind the predictions from direct Voyager imaging. It is as bright as expected based on Voyager photometry (Karkoschka 2001a) using a phase curve of ring particles.

Cordelia is detectable exactly at the position predicted by French and Nicholson (1995 and personal communication, 2000) near the expected signal level. This is well within Owen and Synnott's error bars, as is the case for their other nine measured satellites. On the other hand, the detection is inconsistent with Jacobson's (1998) uncertainty. The new detections of Cordelia and Ophelia give opposition magnitudes (Table IV) 0.7 mag brighter than previously estimated by Thomas *et al*. (1989).

S/1986 U 10 is not uniquely detectable. The highest possible signal is close to the expected one, but there are a few other possibilities with slightly less signal (cf. to the highest peaks at the bottom of Fig. 12). The next HST observation with a similar exposure level will probably clarify the current ambiguity. Most of the detected signal comes from two 2-minute integrations in the 1.59 μm filter. Thus, HST is capable of detecting the faintest uranian satellites with short integrations.

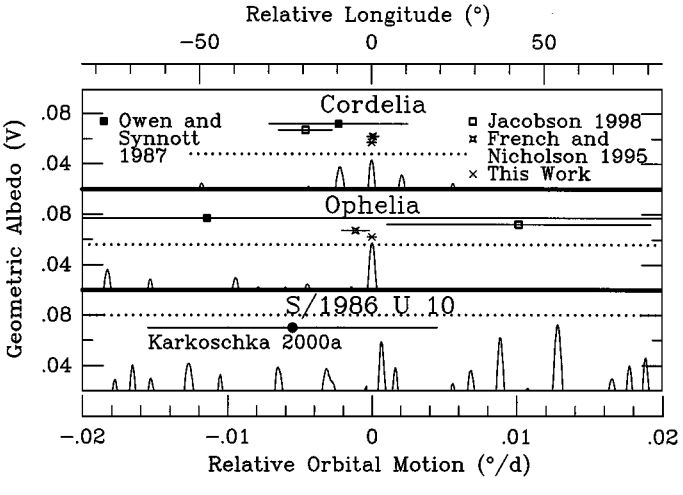

FIG. 12. Measured signal of the three faintest satellites as a function of their assumed mean motions, displayed as curves. Expected signals based on Voyager data and assumed phase functions are displayed as dotted lines. Positional uncertainty ranges of previously determined mean motions are shown. The zero point for the mean motions are the adopted values for Cordelia (1054.5229 ± 0.0003°/d) and Ophelia (956.4182 ± 0.0003°/d), and the 44 : 43 eccentric resonance of S/1986 U 10 with Belinda (564.2461°/d).

XI. SUMMARY

This work presents a photometric data set for 4 uranian rings and 16 uranian satellites, based on HST images taken in 1997. The wavelength range is 0.27–2 μm with up to 25 different filters per object. Phase angles extend over the whole range accessible from Earth (0.03–3°). This is the most extensive photometric data set on uranian rings and satellites aside from the Voyager data set which is complementary to the new data.

The new data is very consistent with previous HST data (Karkoschka 1997) and Voyager data (Ockert *et al*. 1987, Thomas *et al*. 1989, and Veverka *et al*. 1987) for similar observational conditions such as wavelength and phase angle. When observational parameters differ, data points can consistently be connected by smooth spectra and phase functions. The agreement with ground-based observations is partial.

For the five major satellites, geometric albedos and opposition magnitudes in the visible have been reported in many publications (Harris 1961, Anderson 1974, Reitsema *et al*. 1978, Brown 1982, Nelson *et al*. 1987, Veverka *et al*. 1987, Helfenstein *et al*. 1988, Goguen *et al*. 1989, Buratti *et al*. 1990, Veverka *et al*. 1991, Buratti *et al*. 1992). The geometric albedos and opposition magnitudes determined in this work are brighter than every previous value for each satellite. While the data at 1–3° phase angles generally agree, the data of this work near 0° show phase curves much steeper than previous extrapolations. Almost half of the data of this work were taken at phase angles below 0.1° where a large part of the opposition surge occurs, but where few Solar System objects have been observed previously. Unless the uranian satellites have very special surfaces, such steep opposition surges may be common among other Solar System objects.

The minor satellites are about twice as bright at opposition as estimated from Voyager data at higher phase angles (Thomas *et al*. 1989) but consistent with previous HST data (Karkoschka 1997). Geometric albedos of ring particles are 60% larger than estimated from Voyager data (Ockert *et al*. 1987) and closer to previous HST data (Karkoschka 1997).

The combined Voyager/HST data set can be fit very well by simple, normalized phase functions with two free parameters. Derived bond albedos mostly agree with previous estimates while the phase integrals are much lower than estimated previously.

Previous investigations used five-parameter Hapke models to fit phase functions for the major satellites and for Voyager's clear filter (Helfenstein *et al*. 1988, Buratti *et al*. 1990, and Skypeck *et al*. 1991). This work built on those results and extends to seven-parameter Hapke models, to minor satellites and ring particles, and to ultraviolet and near-infrared wavelengths. Good fits can be achieved by setting four parameters constant with almost perfect correlations between the other three parameters, the size and width of the shadow-hiding opposition surge parameters and the single scattering albedo of surface grains. Possible exceptions are Titania and Oberon which deviate slightly from the correlations.

The new data show a distinction in the surfaces between Puck and the Portia group which is different from the original Voyager analysis (Thomas *et al*. 1989) but consistent with the reanalysis by Karkoschka (2001a).

The small amplitude of predicted rotational light curves of the major satellites was based on Voyager data. A large amplitude was observed for Juliet, Portia, and Belinda and interpreted to be due to their oblong shape. The implied satellite shapes are consistent with those measured in resolved Voyager images (Karkoschka 2001a). The data were tested for the presence of albedo features on the minor satellites and for a north–south albedo asymmetry on major satellites. None was found.

The small, faint satellites Cordelia and Ophelia were recovered, improving the uncertainty of their motion by 1–2 orders of magnitude. Both satellites were found at longitudes predicted by French and Nicholson (1995) based on the satellite's gravitational interaction with the ε ring. This finding supports the theory that they are shepherding the ε ring.

The uranian satellites have various, subtle colors, as determined before (Karkoschka 1997), with spectral slopes independent of wavelength, aside from absorptions. The water ice absorptions at 1.5-2 μm wavelength were confirmed and quantified. A small water ice absorption was found in Puck's spectrum. It may also be present in spectra of the Portia group. However, the ring spectrum is flat, consistent with Baines *et al*. (1998).

The photometric model (Section IV) and its parameters (Table VII) define the reflectivity of 20 members of the uranian system for all orbital longitudes, for all phase angles observable from Earth (and higher phase angles), and for a wide range of wavelengths, based on observations at $-40°$ subsolar latitude. The brightness can be expressed in magnitudes in various spectral bands with the help of Tables IV and VIII. The same model and parameters also fit Voyager data at $-82°$ subsolar latitude, but they may not be suitable for near-equatorial viewing geometries.

Essentially all of our data on the uranian system were acquired during the past 25 years, when the sun was shining on Uranus from high southern latitudes, during which time only small changes in both the viewable area and observed photometry occurred. On the other hand, during the next 15–20 years, the uranian system will go through low subsolar latitudes with the likelihood of more pronounced photometric variations. During this time period, prolate shapes and longitudinal albedo features produce the largest amplitudes in rotational lightcurves, and latitudinal albedo features cause the fastest albedo change, which will undoubtedly produce some surprising results.

ACKNOWLEDGMENTS

I thank Martin Tomasko, principal investigator of the HST observations, for his support and his suggestions on the manuscript. The staff of STScI was very cooperative given tight scheduling constraints for the HST observations. The tremendously constructive review by Kevin Baines is especially acknowledged. Support for this work was provided by NASA through Grant GO-07429.01-96A from the Space Telescope Science Institute, which is operated by the Association of Universities for Research in Astronomy, Inc., under NASA Contract NAS5-26555.

REFERENCES

Anderson, L. E. 1974. *A Photometric Study of Pluto and Satellites of the Outer Planets*. Ph.D. thesis, Univ. of Indiana, Bloomington.

Axon D., W. Baggett, C. Blades, H. Bushouse, D. Daou, R. Gilliland, R. Kutina, C. Ritchie, and M. Stevens 1996. *NICMOS Instrument Handbook*. Space Telescope Science Institute, Baltimore.

Baggett, S., and S. Gonzaga 1998. WFPC2 long-term photometric stability. Instrument Science Report WFPC2 98-03. Space Telescope Science Institute, Baltimore.

Baines, K. H., P. A. Yanamandra–Fischer, L. A. Lebofsky, T. W. Momary, W. Golisch, C. Kaminski, and W. J. Wild 1998. Near-infrared absolute photometric imaging of the uranian system. *Icarus* **132**, 266–284.

Biretta, J., C. Burrows, J. Holtzman, I. Heyer, M. Stevens, S. Baggett, S. Casertano, M. Clampin, A. Fruchter, H. Ferguson, R. Gilliland, R. Griffiths, J. Krist, K. Noll, C. O'Dea, M. Stiavelli, A. Suchkov, J. Surdej, and B. Whitmore 1996. *WFPC2 Instrument Handbook, Version 4.0*. Space Telescope Science Institute, Baltimore.

Brown, R. H. 1982. *The Satellites of Uranus: Spectrophotometric and Radiometric Studies of Their Surface Properties and Diameters*. Ph.D. thesis, Univ. of Hawaii, Honolulu.

Brown, R. H., and D. P. Cruikshank 1983. The uranian satellites: Surface compositions and opposition brightness surges. *Icarus* **55**, 83–92.

Buratti, B., F. Wong, and J. Mosher 1990. Surface properties and photometry of the uranian satellites. *Icarus* **84**, 203–214.

Buratti, J. B., J. Gibson, and J. A. Mosher 1992. CCD photometry of the uranian satellites. *Astron. J.* **104**, 1618–1622.

Clark, R. N., R. H. Brown, P. D. Owensby, and A. Steele 1984. Saturn's satellites: Near-infrared spectrophotometry (0.65–2.5 μm) of the leading and trailing sides and compositional implications. *Icarus* **58**, 265–281.

Clark, R. N., and P. G. Lucey 1984. Spectral properties of ice–particulate mixtures and implications for remote sensing. 1. Intimate mixtures. *J. Geophys. Res.* **83**, 2597–2602.

Colina, L., R. C. Bohlin, and F. Castelli 1996. The 0.12–2.5 μm absolute flux distribution of the sun for comparison with solar analog stars. *Astron. J.* **112**, 307–315.

Davies, M. E., V. K. Abalakin, A. Brahic, M. Bursa, B. H. Chovitz, J. H. Lieske, P. K. Seidelmann, A. T. Sinclair, and Y. S. Tjuflin 1992. Report of the IAU/IAG/COSPAR working group on cartographic coordinates and rotational elements of the planets and satellites: 1991. *Celest. Mech. Dynam. Astron.* **53**, 377–397.

Dickinson, M. 1999. *NICMOS Data Handbook Version 4.0*. Space Telescope Science Institute, Baltimore.

French, R. G., and P. D. Nicholson 1995. Edge waves and librations in the Uranus ε ring. *Bull. Am. Astron. Soc.* **27**, 1205.

Gehrels, T., and E. F. Tedesco 1979. Minor planets and related objects. XXVIII. Asteroid magnitudes and phase relations. *Astron. J.* **84**, 1079–1087.

Gladman, B. J., P. D. Nicholson, J. A. Burns, J. J. Kavelaars, B. G. Marsden, G. V. Williams, and W. B. Offutti 1998. Discovery of two distant irregular moons of Uranus. *Nature* **392**, 897–899.

Goguen, J. D., H. B. Hammel, and R. H. Brown 1989. V photometry of Titania, Oberon, and Triton. *Icarus* **77**, 239–247.

Hapke, B. 1984. Bidirectional reflection spectroscopy. 3. Correction for macroscopic roughness. *Icarus* **59**, 41–59.

Hapke, B. 1998. A revised bidirectional reflectance function for planetary regoliths. *Bull. Am. Astron. Soc.* **30**, 1080.

Harris, D. L. 1961. Photometry and colorimetry of planets and satellites. In *Planets and Satellites* (G. P. Kuiper and B. M. Middlehurst, Eds.), pp. 272–342. The University of Chicago Press, Chicago.

Hayes, D. S. 1985. Calibration of fundamental quantities, in *Proceedings of IAU Symposium No. 111*, edited by D. S. Hayes, L. E. Pasinetti, and A. G. Davies Phillip. Reidel, Dordrecht.

Helfenstein, P., J. Veverka, and P. C. Thomas 1988. Uranus satellites: Hapke parameters from Voyager disk-integrated photometry. *Icarus* **74**, 231–239.

Helfenstein, P., N. Currier, B. E. Clark, J. Veverka, M. Bell, R. Sullivan, J. Klemaszewski, G. Greeley, R. T. Pappalardo, J. W. Head III, T. Jones, K. Klaasen, K. Magee, P. Geissler, R. Greenberg, A. McEwen, C. Phillips, T. Colvin, M. Davies, T. Denk, G. Neukum, and M. J. S. Belton 1998. Galileo observations of Europa's opposition effect. *Icarus* **135**, 41–63.

Herbst, T. M., M. F. Skrutskie, and P. D. Nicholson 1987. The near-infrared phase curve of the uranian rings. *Icarus* **71**, 103–114.

Jacobson, R. A. 1998. The orbits of the inner uranian satellites from Hubble Space Telescope and Voyager 2 observations. *Astron. J.* **115**, 1195–1999.

Karkoschka, E. 1997. Rings and satellites of Uranus: Colorful and not so dark. *Icarus* **125**, 348–363.

Karkoschka, E. 1998a. Clouds of high contrast on Uranus. *Science* **280**, 570–572.

Karkoschka, E. 1998b. *WFPC2 Photometry for Solar System Objects*. Space Telescope Science Institute, Baltimore. http://www.stsci.edu/instruments/wfpc2/Wfpc2_phot/wfpc2_ss_phot.html.

Karkoschka, E. 1998c. Methane, ammonia, and temperature measurements of the jovian planets and Titan from CCD-spectrophotometry. *Icarus* **133**, 134–146.

Karkoschka, E. 2001a. Voyager's eleventh discovery of a satellite of Uranus and photometry and the first size measurements of nine satellites. *Icarus* **151**, 69–77.

Karkoschka, E. 2001b. Photometric modeling of the epsilon ring of Uranus and its spacing of particles. *Icarus* **151**, 78–83.

Keyes, T. 1997. *HST Data Handbook, Version 3.0*. Space Telescope Science Institute, Baltimore.

Krist, J. 1994. *The Tiny Tim User's Manual, Version 4.0*. Space Telescope Science Institute, Baltimore.

Lockwood, G. W., and D. T. Thompson 1999. Photometric variability of Uranus, 1972–1996. *Icarus* **137**, 2–12.

Lucy, L. B. 1974. An iterative technique for the rectification of observed distributions. *Astrophys. J.* **79**, 745.

Magain, P., F. Courbin, and S. Sohy 1997. Deconvolution with correct sampling. *ESO Messenger* **88**, 28–31.

Mishchenko, M. I. 1992. The angular width of the coherent backscatter opposition effect: An application to icy outer planet satellites. *Astrophys. Space Sci.* **194**, 327–333.

Nelson, M. R., B. J. Buratti, B. D. Wallis, A. L. Lane, R. A. West, K. E. Simmons, C. W. Hord, and L. W. Esposito 1987. Voyager 2 photopolarimeter observations of the uranian satellites. *J. Geophys. Res.* **92**, 14,905–14,910.

Nicholson, P. D., T. J. Jones, and K. Matthews 1982. Infrared observations of the uranian rings. *IAU Colloquium No. 75*.

Ockert, M. E., J. N. Cuzzi, C. C. Porco, and T. V. Johnson 1987. Uranian ring photometry: Results from Voyager 2. *J. Geophys. Res.* **92**, 14,969–14,978.

Owen, W. M., Jr., and S. P. Synnott 1987. Orbits of the ten small satellites of Uranus. *Astron. J.* **93**, 1268–1271.

Pascu, D., J. R. Rohde, P. K. Seidelmann, E. Wells, C. Kowal, A. Storrs, B. Zellner, D. G. Currie, and D. M. Dowling 1995. HST photometry of the uranian inner satellite system. *Bull. Am. Astron. Soc.* **27**, 1169–1170.

Porco, C. C., J. N. Cuzzi, M. E. Ockert, and R. J. Terrile 1987. The color of the uranian rings. *Icarus* **72**, 69–78.

Reitsema, H. J., B. A. Smith, and D. E. Westrop 1978. Visual and infrared photometry of uranian satellites. *Bull. Am. Astron. Soc.* **10**, 585.

Roush, T. L., D. P. Cruikshank, T. C. Owen, T. R. Geballe, G. K. Benedix, C. de Bergh, K. S. Noll, and B. N. Khare 1998. Titania and Oberon: Surface composition from new near-infrared observations and reflectance models. *Bull. Am. Astron. Soc.* **30**, 1100.

Skypeck, A., J. Veverka, P. Helfenstein, and L. Baker 1991. The photometric roughness of Ariel is not unusual. *Icarus* **90**, 181–183.

Tholen, D. J., and M. W. Buie 1997. Bulk properties of Pluto and Charon. In *Pluto and Charon* (S. A. Stern and D. J. Tholen, Eds.), pp. 193–219. Univ. of Arizona Press, Tucson.

Thomas, P. C. 1988. Shapes of small satellites. *Icarus* **77**, 248–274.

Thomas, P., C. Weitz, and J. Veverka 1989. Small satellites of Uranus: Disk-integrated photometry and estimated radii. *Icarus* **81**, 92–101.

Trauger, J. T., A. H. Vaughan, R. W. Evans, and D. C. Moody 1995. Geometry of the WFPC2 focal plane. In *Calibrating Hubble Space Telescope: Post Servicing Mission* (A. Koratkar and C. Leitherer, Eds.), pp. 379–385. Space Telescope Science Institute. Baltimore.

Veverka, J., P. Thomas, and P. Helfenstein 1987. Satellites of Uranus: Disk-integrated photometry from Voyager imaging observations. *J. Geophys. Res.* **92**, 14,895–14,904.

Veverka, J., R. H. Brown, and J. F. Bell 1991. Uranus satellites: Surface properties. In *Uranus* (J. T. Bergstralh, E. D. Miner, and M. S. Matthews, Eds.), pp. 528–560. Univ. of Arizona Press, Tucson.

Wagener, R., J. Caldwell, and K.-H. Fricke 1986. The geometric albedos of Uranus and Neptune between 2100 and 3350 Å. *Icarus* **67**, 281–288.

Whitmore, B. 1998. *Time Dependence of the Charge Transfer Efficiency on the WFPC2*. Technical Instrument Report WFPC2 98-01. Space Telescope Science Institute, Baltimore.

Whitmore, B., and I. Heyer 1997. *New Results on CTE and Constraints on Flat-Filed Accuracy*. Instrument Science Report WFPC2 97-08. Space Telescope Science Institute, Baltimore.